

# Broadband Vibrational Energy Harvesting Based on a Triboelectric Nanogenerator

Jin Yang, Jun Chen, Ya Yang, Hulin Zhang, Weiqing Yang, Peng Bai, Yuanjie Su, and Zhong Lin Wang\*

Vibrations in living environments are generally distributed over a wide frequency spectrum and exhibit multiple motion directions over time, which renders most of the current vibration energy harvesters unpractical for their harvesting purposes. Here, a 3D triboelectric nanogenerator (3D-TENG) is designed based on the coupling of the triboelectrification effect and the electrostatic induction effect. The 3D-TENG operates in a hybridization mode of conjuncting the vertical contact-separation mode and the in-plane sliding mode. The innovative design facilitates harvesting random vibrational energy in multiple directions over a wide bandwidth. An analytical model is established to investigate the mechano-triboelectric transduction of 3D-TENG and the results agree well with experimental data. The 3D-TENG is able to harvest ambient vibrations with an extremely wide working bandwidth. Maximum power densities of  $1.35 \text{ W m}^{-2}$  and  $1.45 \text{ W m}^{-2}$  are achieved under out-of-plane and in-plane excitation, respectively. The 3D TENG is designed for harvesting ambient vibration energy, especially at low frequencies, under a range of conditions in daily life and has potential applications in environmental/infrastructure monitoring and charging portable electronics.

## 1. Introduction

Over the past decades, harvesting ambient environmental energy has attracted increasing interest for realizing self-powered systems and for meeting large-scale energy demands. Searching for clean and renewable energy with reduced carbon emissions is urgent to the sustainable development of human civilization.<sup>[1]</sup> To date, various energy harvesters for scavenging ambient environmental vibrational energy have been developed that rely on piezoelectric,<sup>[2–6]</sup> electromagnetic,<sup>[7,8]</sup>

and electrostatic<sup>[9,10]</sup> transduction mechanisms. Considerable research effort has been devoted to improve the efficiency of vibrational energy harvesters.<sup>[11–18]</sup> However, regardless of the transduction mechanisms and novel structures, the vibration-to-electric conversion efficiency is still quite low in the existing harvesters because: 1) most of them are designed as linear resonant structures in order to achieve maximum power generation, which limits their application in real-world environments with stochastic or varying vibration spectra;<sup>[14]</sup> and 2) most devices can only effectively harvest vibrational energy from a single motion direction and/or within a small bandwidth. In this case, the harvesters are not effective at scavenging energy from a vibration with multiple or time-variant motion directions.<sup>[11,12,14]</sup>

Recently, the innovative triboelectric nanogenerator (TENG) has offered a cost-effective, simple, and robust approach to convert mechanical energy into electricity based on the coupling between triboelectrification and electrostatic induction.<sup>[19–27]</sup> The triboelectrically charged planes of TENGs change the electric polarization and field across two electrodes by either periodic vertical contact separation<sup>[19–21]</sup> or in-plane sliding,<sup>[22,23]</sup> leading to an alternating flow of electrons through the external load. The developed TENGs have been successfully applied as sustainable power sources for portable electronics,<sup>[21]</sup> magnetic sensors,<sup>[24]</sup> environmental monitors,<sup>[25]</sup> and other self-powered systems.<sup>[26,27]</sup>

Here, we demonstrated a newly designed 3D-TENG that is able to scavenge vibrational energy in the out-of-plane direction and arbitrary in-plane directions with considerable wide bandwidth. It works in a hybridized mode of both vertical contact separation and in-plane sliding. Under out-of-plane motion excitation, the 3D-TENG produces an open-circuit voltage up to 123 V, a peak short-circuit current density of  $30 \text{ mA m}^{-2}$ , and a peak power density of  $1.35 \text{ W m}^{-2}$ . The corresponding electrical outputs are 143 V,  $32 \text{ mA m}^{-2}$ , and  $1.45 \text{ W m}^{-2}$ , respectively, when the 3D-TENG works under in-plane motion excitation. The remarkable performance enables the 3D-TENG to have tremendous practical applications including harvesting wind- or rain-droplet-induced vibrational energy from the national grid transmission lines, natural vibration energy from human walking, and rotation energy from vehicles with wheels.

Dr. J. Yang, J. Chen, Dr. Y. Yang, H. L. Zhang,  
Dr. W. Q. Yang, P. Bai, Y. J. Su, Prof. Z. L. Wang  
School of Materials Science and Engineering  
Georgia Institute of Technology  
Atlanta, Georgia, 30332–0245, USA  
E-mail: zlwang@gatech.edu

Dr. J. Yang  
Department of Optoelectronic Engineering  
Chongqing University  
Chongqing, 400044, P. R. China  
Prof. Z. L. Wang  
Beijing Institute of Nanoenergy and Nanosystems  
Chinese Academy of Sciences  
Beijing, 100083, China



DOI: 10.1002/aenm.201301322

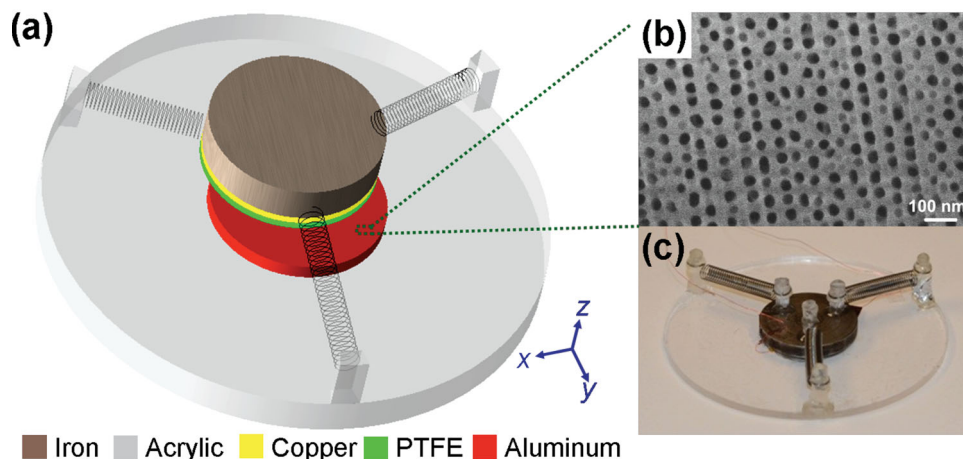


**Figure 1.** 3D triboelectric nanogenerator: a) schematic of a 3D-TENG; b) SEM image of nanopores on an aluminum electrode; and c) a photograph of the fabricated 3D-TENG.

## 2. Design and Analysis

The 3D-TENG has a multilayer structure with circular acrylic as supporting substrates, as shown schematically in **Figure 1a**. The cylindroid core of the 3D-TENG lies at the center of the acrylic substrate with a bottom diameter of 3 cm. On the top of the core, an iron mass is mobile and suspended by three identical springs with an included angle of  $120^\circ$  between each other. The designed structural symmetry ensures that the whole system has a constant resonant frequency in arbitrary in-plane directions. A layer of polytetrafluoroethylene (PTFE) film as one contact surface was adhered onto the bottom side of circular iron mass with a deposited copper thin film as the back electrode. Attached to the bottom acrylic substrate, an aluminum thin film with nanopore modification plays dual roles as a contact electrode and the other contact surface. The scanning electron microscopy (SEM) images of aluminum nanopores are shown in **Figure 1b** and Supporting Information **Figure S1**.

The nanopores were uniformly distributed on the surface of aluminum foil with an average diameter of 30 nm. The average depth of the aluminum nanopores is  $0.7 \mu\text{m} \pm 0.2 \mu\text{m}$  with a distribution density of 290 per  $\mu\text{m}^2$ , which is able to largely increase the effective contact area, thus the electric output of the 3D-TENG. **Figure 1c** shows a photograph of the real 3D-TENG device. Detailed fabrication specifications are reported in the Experimental Section.

A cycle of the electricity generation process of the 3D-TENG is illustrated in **Figure 2**. Two working modes are depicted: vertical contact-separation mode (**Figure 2a**) and in-plane sliding mode (**Figure 2b**). To operate and investigate the vertical contact separation mode, the bottom acrylic substrate of the 3D-TENG is attached to an external vibration source. At original position in **Figure 2a**, the PTFE layer fully contacts with the aluminum thin film. Because PTFE is much more triboelectrically negative than aluminum, electrons are injected from aluminum into PTFE, generating positive triboelectric charges

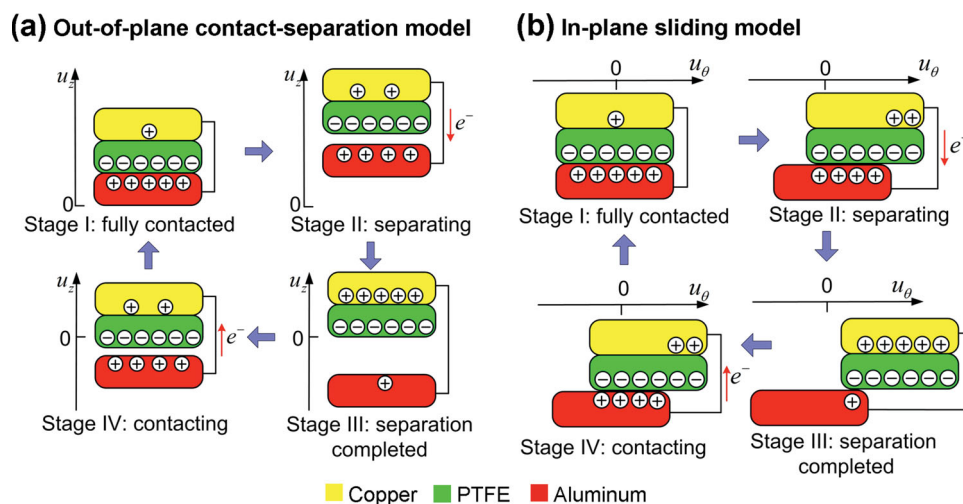


**Figure 2.** Two cycles of the electricity generation process, illustrating the working mechanism of the 3D-TENG: a) vertical contact separation mode and b) in-plane sliding mode.

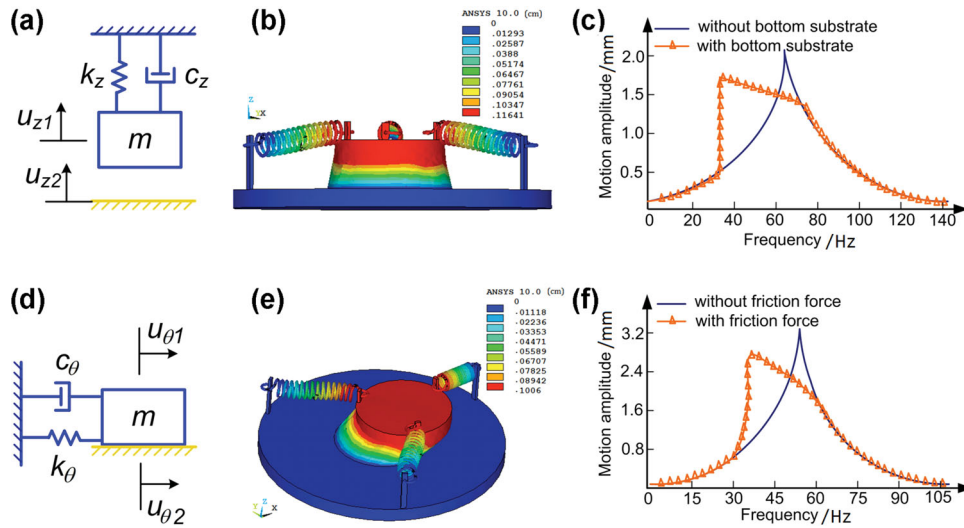


**Figure 3.** Simulation of the 3D-TENG. a) Analytical model for the vertical contact separation mode. b) Instant motion state result of the vertical contact separation mode by ANSYS. c) Simulated frequency response of the vertical contact separation mode with increased working bandwidth. d) Analytical model for in-plane sliding mode. e) Instant motion state result of the in-plane sliding mode by ANSYS. f) Simulated frequency response of the in-plane sliding mode with increased working bandwidth.

on the aluminum side and negative charges on the PTFE side (Figure 2a, Stage I). Once an external vibration force acts on the 3D-TENG along the  $z$ -axis, the supporting substrate and the mass move upward simultaneously. An electric potential difference is not established until a separation emerges when the acrylic substrate reaches its maximum amplitude and right starts to move downward. Meanwhile, the iron mass continues to move upwards due to its inertia (Figure 2a, Stage II). Such an electric potential difference will drive the flow of electrons from the copper electrode to the aluminum electrode through the external circuit, screening the positive triboelectric charges on the aluminum electrode. The electric potential difference is a monotonically increasing function of the separation, and both of them are maximized when the acrylic supporting substrate reaches its lowest point. At this moment, most of the positive triboelectric charges are naturalized (Figure 2a, Stage III). When the iron mass moves downward, the approach of the two contact surfaces results in another electric potential difference in a reversed manner (Figure 2a, Stage IV), which drives the electrons flow from the aluminum electrode to the copper electrode. Most of the positive charges on the copper electrode will be transferred back to the aluminum electrode at the moment when the two surfaces impact each other (Figure 2a, Stage I).

The working mechanism of the in-plane sliding mode is schematically depicted in Figure 2b. At original position, the PTFE film fully contacts with the aluminum thin film, creating positive triboelectric charges on the aluminum side and negative charges on the PTFE side (Figure 2b, Stage I). Once the top contact surface moves along arbitrary in-plane direction and a displacement is established relative to the substrate, the uncompensated negative triboelectric charges on PTFE will repulsively drive free electrons on the copper electrode to the aluminum electrode, screening the positive triboelectric charges and leaving behind positive inductive charges (Figure 2b, Stage II). The flow of inductive electrons lasts until the relative

displacement reaches the maximum (Figure 2b, Stage III). Therefore, at this fully displaced position, most of the positive triboelectric charges are neutralized by the inductive electrons, indicating that no more current flows in the external circuit. Subsequently, as the displacement is decreased by the reciprocating force, the inductive electrons flow back to the copper electrode from the aluminum electrode (Figure 2b, Stage IV) until the fully aligned position is recovered (Figure 2b, Stage I). Therefore, in the entire in-plane sliding process, an alternating current is produced in the external circuit. In both vertical contact separation mode and in-plane sliding mode, the 3D-TENG acts as a charge pump to drive the electrons flowing back and forth in an alternating manner, generating alternating current through the external load.

When the 3D-TENG works in the vertical contact separation mode, a vibration-impacting model can be applied to analyze the frequency characteristics of the 3D-TENG, as illustrated in Figure 3a, which consists of a movable mass  $m$  suspended by a spring  $k_z$  and a damper  $c_z$ . In this model, an external excitation  $u_{z2}$  through the acrylic substrate causes the iron mass to vibrate relative to the substrate  $u_{z1}$ . The differential equation of motion can be written as<sup>[28]</sup>

$$\ddot{u}_z + 2\xi_z \dot{u}_z + u_z = \rho^2 \sin(\rho\pi) + f(u_z, \dot{u}_z) \quad (1)$$

where,  $\ddot{u}_z$  and  $\dot{u}_z$  are the relative acceleration and velocity of the mass with respect to the substrate,  $u_{z2} = U_z \sin(\omega t)$ ,  $U_z$  is the amplitude of the external excitation,  $u_z = u_{z1}/U_z$ ,  $\xi_z$  is the primary suspension damping characteristic and defined as  $\xi_z = c_z/(2m\omega_0)$ ,  $\rho = \omega/\omega_0$ ,  $f(u_z, \dot{u}_z) = \begin{cases} 0 & (u_z > 0) \\ -2\rho\xi_z\dot{u}_z - \rho^2u_z & (u_z < 0) \end{cases}$ ,  $\omega_0 = \sqrt{k_z/m}$ , and  $\omega$  is the excitation frequency. It can be found that, this impact between the mass and substrate introduces a nonlinear function  $f(u_z, \dot{u}_z)$  of  $u_z$  and  $\dot{u}_z$  into the motion model, leading to a different frequency response compared to the linear model. Similarly, a motion model of the 3D-TENG under in-plane excitation is developed and illustrated in Figure 3d, where

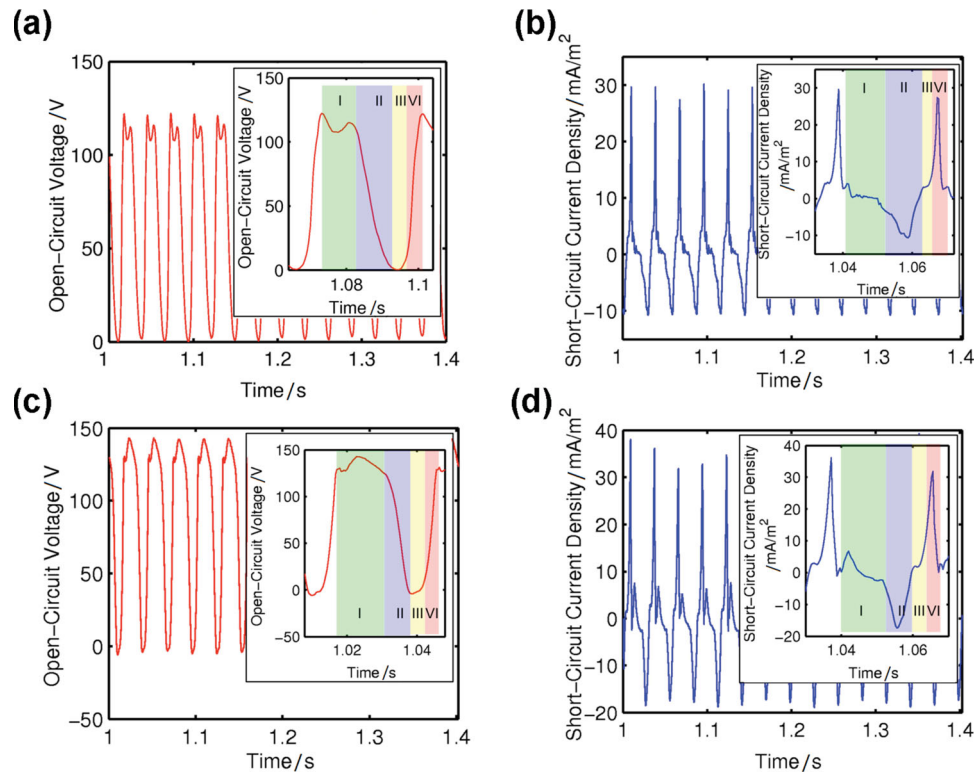


**Figure 4.** Electrical output measurements of the 3D-TENG. a) Open-circuit voltage and b) short-circuit current density under out-of-plane excitation with a vibrational frequency of 36 Hz. c) Open-circuit voltage and d) short-circuit current density at an in-plane excitation angle of  $180^\circ$  with a vibrational frequency of 36 Hz.

$k_\theta$  and  $c_\theta$  denote the stiffness and damper of the system along arbitrary in-plane angle of  $\theta$ .  $u_{\theta 2}$  is the displacement of the substrate, defined as  $u_{\theta 2} = U_\theta \sin(\omega t)$ , and  $u_{\theta 1}$  is the relative displacement of the mass to the substrate. The differential equation of in-plane motion along  $\theta$  is written as<sup>[29]</sup>

$$\ddot{u}_\theta + 2\xi_\theta \dot{u}_\theta + u_\theta = \rho_\theta^2 \sin(\rho_\theta \pi) - f_{\text{Fric}} \quad (2)$$

where  $\ddot{u}_\theta$  and  $\dot{u}_\theta$  are the relative acceleration and velocity of the mass with respect to the substrate along excitation angle of  $\theta$ ,  $u_\theta = u_{\theta 1}/U_\theta$ ,  $\rho_\theta = \omega/\omega_{\theta 0}$ ,  $\xi_\theta = c_\theta/(2m\omega_{\theta 0})$ ,  $\omega_{\theta 0} = \sqrt{k_\theta/m}$ ,  $f_{\text{Fric}} = \alpha \dot{u}_\theta/mk_\theta$ , and  $\alpha$  is the coefficient of friction. Due to the friction force, the new damping  $\xi_\theta$  ratio of the in-plane motion will increase and can be expressed as

$$\zeta_\theta = \frac{c_\theta + \alpha}{2\sqrt{k_\theta m}} \quad (3)$$

In this case, the mechanical quality factor  $Q$  ( $Q = 1/2\zeta_\theta$ ), which is inversely proportional to the damping ratio  $\zeta_\theta$ , will decrease with the increase of  $\zeta_\theta$  due to the additional contribution from  $\alpha$ . The introduction of the coefficient of friction  $\alpha$  results in a smaller quality factor and thus a wider working bandwidth.<sup>[30]</sup>

According to Equations (1) and (2), finite element analysis was performed to validate the motion behaviors of the 3D-TENG under the out-of-plane and in-plane excitations. In the simulation, Young's modulus and Poisson's ratio of the spring were 2.1 GPa and 0.26, respectively. Figure 3b shows

an instant motion state when the substrate and iron mass separate from each other under out-of-plane excitation, while Figure 3c demonstrates the frequency responses of the out-of-plane motions with and without the substrate. An intensely nonlinear behavior appears in the frequency response with the substrate due to the vibration-impacting motion, while an obvious linear response is observed in the frequency response without the substrate. The simulations show that the impact motion of iron mass follows a linear frequency response in a certain frequency range, then the motion magnitude jumps to a high level, leading to an increase of working bandwidth on one side of the frequency response. Figure 3e shows an instant motion state when the iron mass slides across the substrate surface under the in-plane excitation. The frequency responses of the in-plane motions with and without the friction force are demonstrated in Figure 3f, which indicate that the working bandwidth is broadened by the friction force. The increased bandwidth is narrower than that by the vibration-impacting mechanism shown in Figure 3c.

### 3. Results and Discussion

To characterize the performance of 3D-TENG, the electrical output measurement was carried out under an average acceleration of  $6 \text{ m s}^{-2}$  generated by a shaker. Figure 4a,b show the open-circuit voltage and short-circuit current density, respectively, under out-of-plane excitation with a vibration frequency

of 36 Hz. An enlarged view of the voltage peak is shown in the inset of Figure 4a. The voltage persists at a plateau of 123 V in Stage I when both the substrate and iron mass move simultaneously upward along the *z*-axis. The voltage gradually decreases during the separation between the substrate and iron mass in Stage II. Then the voltage reaches its minimum at the maximum separation (Stage III). Subsequently, the voltage rapidly rises when the substrate and mass begin to impact together (Stage IV) and reach a plateau value of 123 V again (Stage I). In addition, an enlarged view of the current density is shown in the inset of Figure 4b. The output current has an alternating behavior with asymmetrical amplitudes, with the larger peak ( $30 \text{ mA m}^{-2}$ ) corresponding to the process in which the two contact surfaces move towards each other, while the smaller one ( $10 \text{ mA m}^{-2}$ ) is generated as the two surfaces move apart. Given the same amount of charge transported back and forth, the faster approach is expected to produce a larger current density peak than the slower separation. The accumulative induced charges of  $0.11 \mu\text{C}$  can be generated within 0.03 s (Supporting Information Figure S2). The experimental data validate the working principle described in Figure 2a.

The open-circuit voltage and short-circuit current density at the in-plane excitation angle of  $180^\circ$  with frequency of 36 Hz were plotted in Figure 4c,d, respectively. In the inset of Figure 4c, considering the accumulation of the triboelectric charges on the surfaces of PTFE and aluminum, the voltage retains at level of 142 V as the substrate and mass move away from equilibrium along the  $180^\circ$  direction simultaneously (Stage I). Then the voltage decreases gradually when the iron mass slides apart across the substrate surface due to the inertia (State II). The voltage decreases to a minimum at the largest displacement (State III). Subsequently, the iron mass slides backward (Stage IV) and the relative displacement begins to decrease, leading to an increase of the voltage. Furthermore, similar to the vertical contact separation mode, given the same amount of charge transported back and forth, the faster sliding backwards is expected to produce a larger current density peak ( $32 \text{ mA m}^{-2}$ ) than the slower sliding apart ( $17 \text{ mA m}^{-2}$ ). As demonstrated in Supporting Information Figure S3, the total accumulated induced charges are similar to each other for different in-plane directions with average induced charges of  $0.13 \mu\text{C}$  within 0.03 s.

For operation, an electrodynamic shaker is employed as the external vibration source with controlled amplitude and acceleration. It provides sinusoidal output with a range of vibrational frequencies from 10 to 140 Hz. The supporting acrylic substrate of the 3D-TENG is anchored on the shaker table to investigate the relationship between the electrical outputs and input frequency when it works in a vertical contact separation mode. As shown in Figure 5a, both the voltage and current present a rapid increase with the increase of frequency from 10 to 36 Hz. The maximum values of the voltage and current, respectively, reach 123 V and  $21 \mu\text{A}$  at the frequency of 36 Hz. Then, the voltage and current both gradually decrease to their minima as the frequency increases from 36 to 140 Hz. As analyzed in Figure 3c, which shows the out-of-plane motion behavior, the separation between the substrate and the iron mass varies with the input frequency. The larger separation at 36 Hz would cause a larger contacting force when the two objects impact together. Since the aluminum surface was patterned with nanopores,

a larger impact will largely increase the effective contact area between the two surfaces, and thus the total electric output. In addition, if the half peak voltage point is adopted as the criteria of the working bandwidth,<sup>[31]</sup> compared with the state-of-the-art vibration harvesters,<sup>[8,9]</sup> 3D-TENG shows an extremely wide working bandwidth up to 75 Hz in a low vibrational frequency range under out-of-plane excitation.

When it comes to the in-plane sliding mode, the electric outputs were measured with the input excitation frequencies in a range from 10 to 55 Hz at different in-plane excitation angles ( $0^\circ$ ,  $45^\circ$ ,  $90^\circ$ ,  $135^\circ$ ,  $180^\circ$ ), as shown in Figure 5b–f. The results prove that the 3D-TENG is capable of harvesting vibrational energy from all of the in-plane directions. Considered the non-ideal experimental factors, such as the variation in the spring stiffness factors and the deviation of the fabricated structure symmetry, the 3D-TENG has almost the same response to the external vibrations at arbitrary in-plane directions. Furthermore, both the voltage and current are maximized at a frequency of 36 Hz at all excitation angles. Slightly nonlinear behavior is observed in all of the output responses, mainly due to the nonlinear topology structure of the spring vibration system. In addition, the 3D-TENG shows a wide working bandwidth of 14.4 Hz in a low vibrational frequency range under the in-plane excitation.

The electrical outputs for a 3D-TENG without nanomaterials surface modification are demonstrated in Supporting Information Figure S4. Compared with the electrical outputs with nanomaterials surface modification, the open-circuit voltages under out-of-plane and in-plane excitations were enhanced 38% and 36% of those of the TENG without nanomaterial surface modification, respectively. The nanomaterial-surface-modification-induced short-circuit current improvement rendered values of 35% and 34%, respectively, under the out-of-plane and in-plane excitations. The current peaks and corresponding induced charges generated in one cycle of the 3D-TENG under out-of-plane excitation at the vibrational frequency of 36 Hz, with and without nanomaterial surface modifications, are plotted in Supporting Information Figure S5. Although the peak values of the currents in the discharge and charge cycles are different from each other, the integration charge over time is almost the same, which means no current leakage exists. In addition, the electrical outputs of the TENG were investigated simultaneously under both out-of-plane and in-plane excitations with different composition motion angles at a constant vibrational frequency of 36 Hz, as shown in Supporting Information Figure S6. At the composition motion angles of  $120^\circ$ ,  $135^\circ$ , and  $150^\circ$ , the open-circuit voltages were 122 V, 125 V, and 124 V, respectively. The corresponding short-circuit current densities were  $31 \text{ mA m}^{-2}$ ,  $33 \text{ mA m}^{-2}$ , and  $33 \text{ mA m}^{-2}$ . Furthermore, for the 3D-TENG at the original position, the upper substrate rests at a critical state where the elastic force from the three identical springs is exactly compensated by the gravitational force from the upper substrate and the two plates just contact each other, which effectively prevents the cancellation effect of the output voltages when the out-of-plane and in-plane excitations emerge simultaneously. The frequency response was also studied under excitations simultaneously coming from out-of-plane and in-plane motions. The working bandwidths of 45 Hz, 39 Hz, and 25 Hz were obtained at the composition motion angles of  $120^\circ$ ,

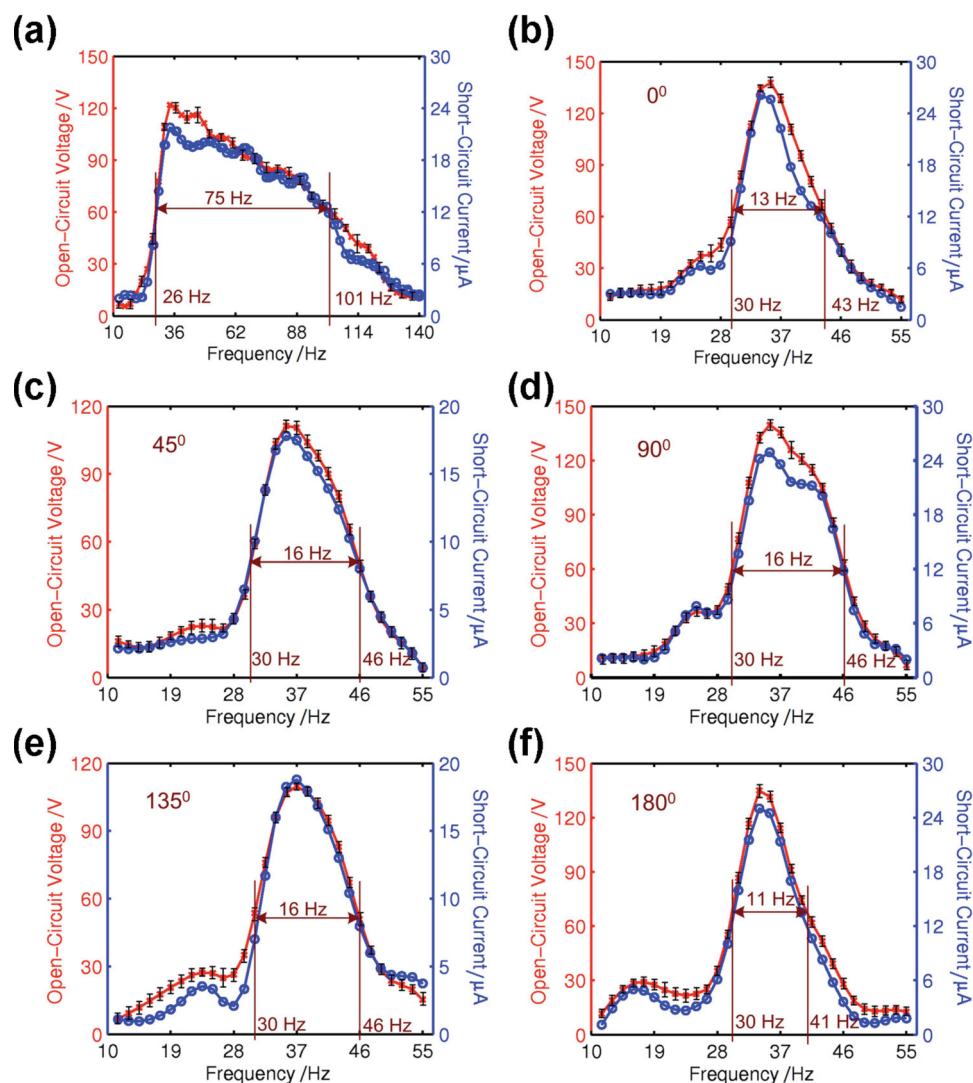


**Figure 5.** Frequency responses of the 3D-TENG. a) Frequency response of 3D-TENG under out-of-plane excitation. b–f) Frequency responses of 3D-TENG at in-plane excitation angles of  $0^\circ$ ,  $45^\circ$ ,  $90^\circ$ ,  $135^\circ$ , and  $180^\circ$ , respectively.

$135^\circ$ , and  $150^\circ$ , respectively. Finally, as demonstrated in Supporting Information Figure S7, the electrical outputs under out-of-plane and in-plane excitations at the third-order, fourth-order, and fifth-order excitation frequencies are low compared with the electrical output under the fundamental excitation frequency. This is because the relative displacement between the iron mass and the bottom substrate decreases under the higher order excitation frequencies, resulting in a significant decrease of output voltage.

Resistors were used as external loads to further investigate the output power of the 3D-TENG at the resonance frequency of 36 Hz. The electrical output measurement was also carried out at an acceleration of  $6 \text{ m s}^{-2}$ , and the input mechanical power is 4 mW at this resonance frequency. As illustrated in Figure 6a, the output current drops with increasing resistance under out-of-plane excitation, while the output voltage followed a reverse trend. Consequently, the instantaneous power density of the external resistance (Figure 6b) reaches a peak value

of  $1.35 \text{ W m}^{-2}$  at a resistance of  $\approx 8.1 \text{ M}\Omega$ . When the device is excited at an arbitrary in-plane angle, the relationship between the output voltages and currents and the resistances are similar to those under the out-of-plane excitation, as demonstrated in Figure 6c,d. The device has the instantaneous peak power density of  $1.45 \text{ W m}^{-2}$  at a resistance of  $\approx 7.9 \text{ M}\Omega$ . With an acceleration of  $6 \text{ m s}^{-2}$  and iron mass of 25 g, the input powers for the 3D-TENG are 2.3 mW and 4.8 mW,<sup>[32,33]</sup> respectively, under the out-of-plane and in-plane excitations. The vibration-to-electric conversion efficiency is 44.7% ( $1.03 \text{ mW}/2.3 \text{ mW}$ ) under the out-of-plane excitation at the resonant frequency of 36 Hz. Likewise, under the in-plane excitation, the average conversion efficiency can be estimated as 24.5% ( $1.18 \text{ mW}/4.8 \text{ mW}$ ). The conversion efficiency of the 3D-TENG under out-of-plane excitation is higher than that of the electrostatic harvester.<sup>[34]</sup> Furthermore, the 3D-TENG is capable of harvesting vibrational energy from different directions, while the electrostatic harvester can only work under the circumstance of single-direction vibration. The

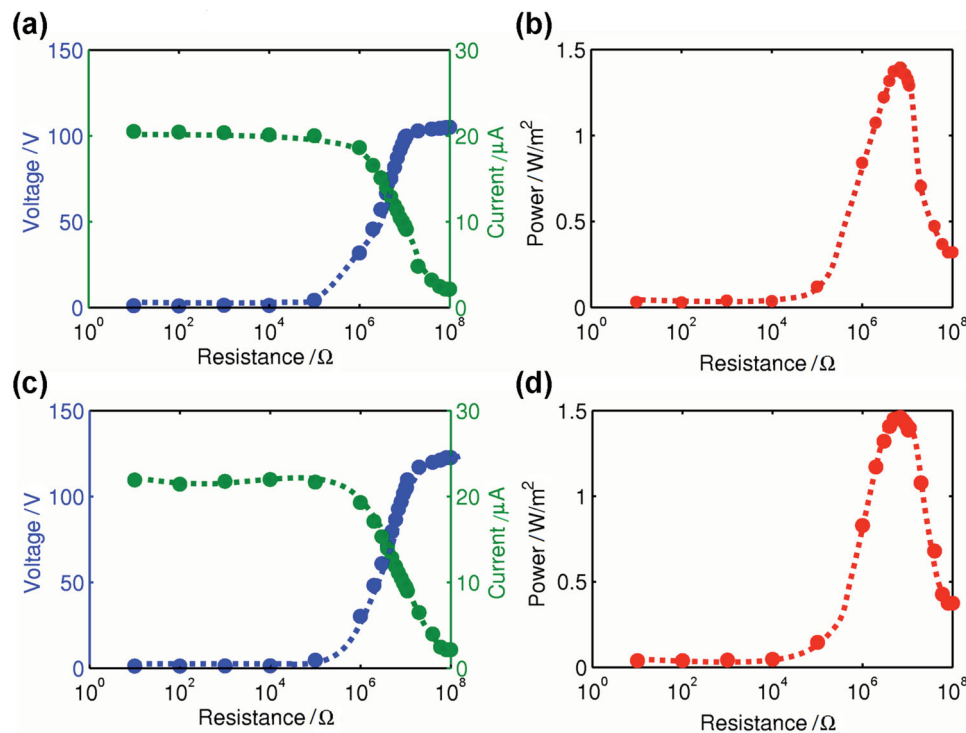


**Figure 6.** Dependence of the voltage and current output on the external load resistance under out-of-plane excitation. The points represent peak values of the electric signals while the lines are the fitted results. b) Dependence of the peak power output on the resistance of the external load under out-of-plane excitation, indicating a maximum power output when  $R = 8.1 \text{ M}\Omega$ . The curve is the fitted result. c) Dependence of the voltage and current output on the external load resistance under in-plane excitation. The points represent peak values of the electric signals while the lines are the fitted results. d) Dependence of the peak power output on the resistance of the external load under in-plane excitation, indicating a maximum power output at  $R = 7.9 \text{ M}\Omega$ .

capacity of energy harvesting is largely limited once the motion direction is diverted for the 1D harvesters. Furthermore, it is worth noting that the energy conversion efficiency of the 1D electrostatic harvester is 23.6% with a bandwidth ratio of 0.1 (half-power bandwidth/ $f_0$ ), which is much narrower than that of the 3D-TENG (0.4) under in-plane excitation.

The practicability of harvesting energy from multiple directions with considerably wide working bandwidth enable the 3D-TENG to have tremendous applications in building self-powered systems by harvesting ambient vibrational energy. To prove the capability of the 3D-TENG as a sustainable power source, three sets of practical applications were demonstrated (see the videos in Supporting Information). First, as shown in **Figure 7a**, the 3D-TENG works on a national grid transmission line that can effectively harvest wind- or rain-droplet-induced line vibrational energy. Forty serial-connected commercial light-emitting diodes (LEDs) were lit by the line oscillating (see Supporting Information Video S1). **Figure 7b** shows the output voltages of the 3D-TENG under different line swing amplitudes. It can be seen that the voltages present an obvious increasing tendency with the increased swing amplitudes. This is because the larger swing amplitude of the line will contribute to a larger out-of-plane separation of the two contact surfaces in the 3D-TENG, leading to a higher output voltage. In addition, the output voltage responding to a range of up-down impact

forces applied onto the line is shown in Supporting Information Figure S8. The 3D-TENG could be applied to monitor the real-time vibration intensity of the transmission line in the national grid or to work as a sustainable power source.

Secondly, shown in **Figure 7c**, the 3D-TENG is mounted on a human leg to harvest the vibration energy from human walking. This human-motion-induced vibration can be used as an external excitation to the 3D-TENG and 40 serial-connected commercial LEDs were lit (see Supporting Information Video S2). **Figure 7d** shows the output voltages under different walk speeds, which indicates that a faster speed leads to a larger voltage output. Furthermore, a frequency information analysis of the generated voltage output signals by Fourier transform is rendered in Supporting Information Figure S9, showing that the main frequency components of the three walking speeds are 2.1 Hz, 3.1 Hz, and 3.9 Hz, respectively.

A third practical application is shown in **Figure 7e**. The 3D-TENG was anchored on a bicycle wheel to harvest the rotation energy and 30 serial-connected commercial LEDs were lit when the wheel rotated (**Figure 7f** and Supporting Information Video S3). This demonstration proves that the 3D-TENG not only can harvest wheel rotation energy but also can be developed as a self-powered sensing system to monitor the tire-pressure of automobiles, airplanes, and other wheel-based vehicles.

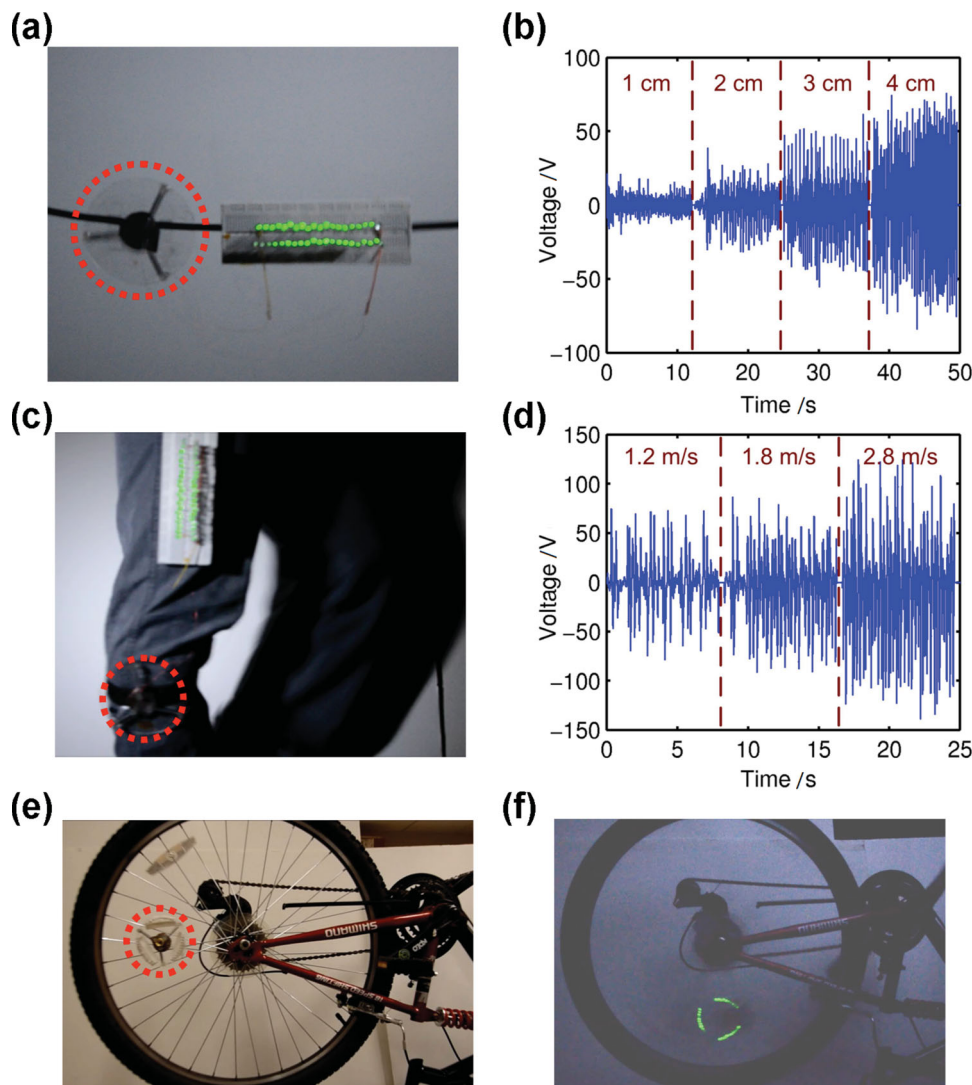


**Figure 7.** Demonstration of the 3D-TENG (marked in red circles) as a sustainable power source and self-powered active sensors. a) Photograph of line vibration energy harvesting. Forty commercial LED bulbs were lit simultaneously. b) The output voltage of the 3D-TENG under different line swing amplitudes. c) Photograph of human-walking energy harvesting. Forty commercial LED bulbs were lit simultaneously. d) The output voltages at different walking speeds. e) Photograph of a 3D-TENG mounted on a still bicycle wheel. f) Thirty commercial LED bulbs were lit simultaneously under the rotation of the bicycle wheel.

#### 4. Conclusion

We have presented an innovative design of a 3D-TENG for effectively harvesting ambient vibrational energy in the out-of-plane direction. It has an extremely wide working bandwidth up to 75 Hz ( $\Delta f/f \approx 1.18$ ) and in arbitrary in-plane directions it has a prepotent bandwidth of 14.4 Hz ( $\Delta f/f \approx 0.38$ ) in the low vibrational frequency range. Maximum power densities of  $1.35 \text{ W m}^{-2}$  and  $1.45 \text{ W m}^{-2}$  were achieved with out-of-plane and in-plane excitations, respectively. The superior vibrational energy harvesting capacity enables the 3D-TENG to have tremendous practical applications, which include harvesting wind- or rain-droplet-induced vibrational energy from the national grid transmission lines, natural vibration energy from human walking, and rotation energy from the wheel-based vehicles. In addition, a large range of self-powered sensing systems

can be also developed due to the 3D-TENG's high sensitivity to external vibrations. This TENG design will find applications in powering portable electronics, environmental/infrastructure monitoring, security, and more.

#### 5. Experimental Section

**Aluminum Nanopore-Based Surface Modification:** Electrochemical anodization was applied on an aluminum foil in 3% (mass fraction) oxalic acid ( $\text{H}_2\text{C}_2\text{O}_4$ ) electrolyte. A platinum plate was used as the cathode. The aluminum foil was anodized under a bias voltage of 30 V for 4 h. The alumina layer was etched away in a solution of  $20 \text{ g L}^{-1}$  chromic acid at  $60 \text{ }^\circ\text{C}$  for 2 h. Then, the aluminum foil was rinsed with deionized (DI) water and dried in air.

**Fabrication of the 3D-TENG:** In the fabrication of the 3D-TENG device, an acrylic substrate with dimensions of  $\Phi = 100 \text{ mm} \times 3 \text{ mm}$

(diameter  $\times$  thickness) was prepared by laser cutter. A iron mass with a diameter of 30 mm and a thickness of 5 mm was suspended by three springs attached to the circular acrylic substrate. The spring had a wire diameter of 0.3 mm, a free length of 14 mm, and outer diameter of 4 mm. A metal electrode was prepared by depositing 100 nm of copper on one side of PTFE film with dimensions of  $\Phi 30$  mm  $\times$  50  $\mu$ m. Then, the copper-coated PTFE was adhered to the bottom surface of the iron mass. The aluminum thin film with nanopores modification was attached to the top acrylic substrate as a contact electrode and the other contact surface.

**Assembly of the Measuring System:** The 3D-TENG was mounted on an electrodynamic shaker (Labworks ET-139) to test the output performances under out-of-plane and in-plane excitations for different frequencies. The shaker was powered by an amplified sinusoidal wave from a function generator (Labworks SC-121) and an amplifier (Labworks Pa-151). The output voltage of the 3D-TENG was measured using a voltage preamplifier (Keithley 6514 System Electrometer). The output current of the 3D-TENG was measured with a low-noise current preamplifier (Stanford Research SR560).

## Supporting Information

Supporting Information is available from the Wiley Online Library or from the author.

## Acknowledgements

J.Y., J.C., and Y.Y. contributed equally to this work. This work was supported by the U.S. Department of Energy, Office of Basic Energy Sciences (DE-FG02-07ER46394), NSF, the Knowledge Innovation Program of the Chinese Academy of Sciences (KJCX2-YW-M13), NSFC (No. 61174017).

Received: August 30, 2013

Revised: October 9, 2013

Published online:

- [1] S. Lee, J. Hong, C. Xu, M. Lee, D. Kim, L. Lin, W. Hwang, Z. L. Wang, *Adv. Mater.* **2012**, *24*, 439.
- [2] Z. L. Wang, J. H. Song, *Science* **2006**, *312*, 242.
- [3] Y. Qin, X. D. Wang, Z. L. Wang, *Nature* **2008**, *451*, 809.
- [4] X. N. Wen, W. Z. Wu, Y. Ding, Z. L. Wang, *Adv. Mater.* **2013**, *25*, 3371.
- [5] Y. F. Hu, L. Lin, Y. Zhang, Z. L. Wang, *Adv. Mater.* **2012**, *24*, 110.
- [6] W. Zeng, X. M. Tao, S. Chen, S. Shang, H. L. W. Chan, S. H. Choy, *Energy Environ. Sci.* **2013**, *6*, 2631.
- [7] S. D. Kwon, J. Park, K. Law, *Smart Mater. Struct.* **2013**, *22*, 055007.
- [8] X. Y. Wang, S. Palagummi, L. Liu, F. G. Yuan, *Smart Mater. Struct.* **2013**, *22*, 055016.
- [9] H. Okamoto, Y. Hamate, L. Xu, H. Kuwano, *Smart Mater. Struct.* **2012**, *21*, 065001.
- [10] Y. Chiu, Y. C. Lee, *J. Micromech. Microeng.* **2013**, *23*, 015012.
- [11] L. C. Rome, L. Flynn, E. M. Goldman, T. D. Yoo, *Science* **2005**, *309*, 1725.
- [12] J. M. Donelan, Q. Li, V. Naing, J. A. Hoffer, D. J. Weber, A. D. Kuo, *Science* **2008**, *319*, 807.
- [13] J. Briscoe, M. Stewart, M. Vopson, M. Cain, P. M. Weaver, S. Dunn, *Adv. Energy Mater.* **2012**, *2*, 1261.
- [14] Z. L. Wang, *Sci. Am.* **2008**, *298*, 82.
- [15] C. Xu, X. D. Wang, Z. L. Wang, *J. Am. Chem. Soc.* **2009**, *131*, 5866.
- [16] Z. G. Yin, Q. D. Zheng, *Adv. Energy Mater.* **2012**, *2*, 179.
- [17] M. Lee, J. Bae, J. Lee, C. S. Lee, S. Hong, Z. L. Wang, *Energy Environ. Sci.* **2011**, *4*, 3359.
- [18] R. Que, Q. Shao, Q. Li, M. Shao, S. Cai, S. Wang, S. T. Lee, *Angew. Chem. Int. Ed.* **2012**, *51*, 5418.
- [19] F. R. Fan, Z. Q. Tian, Z. L. Wang, *Nano Energy* **2012**, *1*, 328.
- [20] S. H. Wang, L. Lin, Z. L. Wang, *Nano Lett.* **2012**, *12*, 6339.
- [21] X. Yang, G. Zhu, S. Wang, R. Zhang, L. Lin, W. Wu, Z. L. Wang, *Energy Environ. Sci.* **2012**, *5*, 9462.
- [22] S. H. Wang, L. Lin, Y. N. Xie, Q. S. Jing, S. M. Niu, Z. L. Wang, *Nano Lett.* **2013**, *13*, 2226.
- [23] L. Lin, S. H. Wang, Y. N. Xie, Q. S. Jing, S. M. Niu, Y. F. Hu, Z. L. Wang, *Nano Lett.* **2013**, *13*, 2916.
- [24] Y. Yang, L. Lin, Y. Zhang, Q. S. Jing, T. C. Hou, Z. L. Wang, *ACS Nano* **2012**, *6*, 10378.
- [25] Z. H. Lin, G. Zhu, Y. Zhou, Y. Yang, P. Bai, J. Chen, Z. L. Wang, *Angew. Chem.* **2013**, *19*, 5065.
- [26] Q. Z. Zhong, J. W. Zhong, B. Hu, Q. Y. Hu, J. Zhou, Z. L. Wang, *Energy Environ. Sci.* **2013**, *6*, 1779.
- [27] G. Zhu, C. F. Pan, W. X. Guo, C. Chen, Y. S. Zhou, R. M. Yu, Z. L. Wang, *Nano Lett.* **2012**, *12*, 4960.
- [28] H. C. Liu, C. K. Lee, T. Kobayashi, C. J. Tay, C. G. Quan, *Smart Mater. Struct.* **2012**, *21*, 035005.
- [29] S. Chatterjee, *Int. J. Nonlin. Mech.* **2007**, *42*, 459.
- [30] A. Erturk, D. J. Inman, *J. Sound Vib.* **2011**, *330*, 2339.
- [31] X. H. Dai, X. D. Miao, L. H. Sui, H. L. Zhou, X. L. Zhao, G. F. Ding, *Appl. Phys. Lett.* **2012**, *100*, 031902.
- [32] E. Halvorsen, *Phys. Rev. E* **2013**, *87*, 042129.
- [33] S. S. Rao, *Mechanical Vibrations* 3rd ed. Addison-Wesley, Reading, MA **1995**.
- [34] C. P. Le, E. Halvorsen, O. Sørasen, E. M. Yeatman, *Smart Mater. Struct.* **2013**, *22*, 075020.